INKJET-PRINTED MAGNETOELECTRIC NANOPARTICLES: DEPOSITION AND CHARACTERIZATION

[1]Vojtěch POVOLNÝ, [1]Alexandr LAPOSA, [1]Jiří KROUTIL, [1]Pavel HAZDRA, [2]Pavel VEVERKA, [2]Lenka KUBÍČKOVÁ, [2]Ondřej KAMAN

[1]Faculty of Electrical Engineering, Czech Technical University in Prague, Prague, Czech Republic, EU, povolvoj@fel.cvut.cz

[2]FZU - Institute of Physics of the Czech Academy of Sciences, Cukrovarnická 10/112, 162 00 Prague 6, Czech Republic, EU

https://doi.org/10.37904/nanocon.2025.5190

Abstract

In this research, the formation of thin layers of magnetoelectric nanoparticles (MENPs) by inkjet print is presented. First, the MENPs based on ≈ 9 nm magnetostrictive $CoFe_2O_4$ ferrite cores coated with ferroelectric $BaTiO_3$ shell ($CoFe_2O_4$@$BaTiO_3$) were synthetized and a stable dispersion suitable for inkjet printing was prepared. Then, printing tests were carried out at resolutions of 1270 dpi, 1680 dpi, and 2540 dpi on glass and PET substrates. To evaluate the effect of the number of printed layers, samples containing 5, 10, and 20 layers were prepared. The aim of this study was to assess the influence of printing parameters and substrate type on the quality and morphology of the resulting films. The printed structures were characterized using atomic force microscopy (AFM), contact profilometry, and optical microscopy. The results demonstrate that both printing resolution and the number of layers affect the final thickness and surface morphology of the printed films, with noticeable differences observed between glass and polymer substrates. The variation in printing resolution and number of deposited layers resulted in film thicknesses ranging from 0.1 ± 0.1 μm (at 1270 dpi) to 4.0 ± 0.9 μm (at 2540 dpi) on PET substrates, and from 0.2 ± 0.08 μm to 4.0 ± 0.05 μm on glass substrates, respectively.

Keywords: Inkjet, magnetoelectric nanoparticles, PET, synthesis, AFM

1. INTRODUCTION

Magnetoelectric nanoparticles (MENPs) have emerged as a multifunctional class of materials designed to exhibit coupling between electric and magnetic order parameters, enabling both electric-field control of magnetization and magnetic-field control of polarisation [1]. Their core–shell architecture typically integrates magnetostrictive and piezoelectric components, generating strain-mediated magnetoelectric (ME) coupling at the nanoscale [2]. Typically, the magnetostrictive core of MENPs is composed of the ferrimagnetic spinel ferrite $CoFe_2O_4$, whereas the ferroelectric $BaTiO_3$ forms the piezoelectric shell. Recent advances in synthesis techniques, such as sol–gel and hydrothermal methods, have enhanced structural control, interfacial quality, and ME coefficients of ME composites [3]. These improvements open a pathway for MENPs to serve as future nanoscale transducers in spintronic, sensing, and biomedical systems [4].In electronics, voltage-controlled magnetic switching in MENPs offers potential for low-power magnetic memory and logic devices [5]. Integration with microelectromechanical systems (MEMS) and flexible substrates has further broadened their technological relevance [6]. Theoretical and computational models have provided insights into interfacial strain transfer and charge–spin–lattice coupling that define ME behaviour [7]. Characterization techniques, including transmission electron microscopy (TEM) and piezoresponse force microscopy (PFM), have been crucial in correlating nanoscale structure with functionality [8].

The dynamic interplay among magnetic, electric, and mechanical degrees of freedom promises to make MENPs a cornerstone for multifunctional nanosystems [9]. Their adaptability across diverse domains positions them as transformative materials for smart sensing, actuation, and energy harvesting [10].

In this work, the synthesis of $CoFe_2O_4$@$BaTiO_3$ nanoparticles and preparation of their printable suspension is presented first, then the structural properties of thin MENP layers deposited by the inkjet-print on rigid (glass) and flexible (PET) substrates are evaluated.

2. MATERIALS AND METHODS / EXPERIMENTAL

2.1. Synthesis of $CoFe_2O_4$@$BaTiO_3$ nanoparticles and preparation of the ink

At first, $CoFe_2O_4$ ferrite nanoparticles were prepared by hydrothermal synthesis. Aqueous solution of stoichiometric amounts of $Co(NO_3)_2$ and $Fe(NO_3)_3$ was precipitated by adjusting pH to 9 by dilute NaOH. The resulting mixture was treated under autogenous pressure at 180 °C for 12 h. The $CoFe_2O_4$ particles were separated by centrifugation, thoroughly washed with water, and dried in vacuo.

The coating of ferrite particles with $BaTiO_3$ was inspired by the procedure according to Kozielski et al. [11]; however, large modifications were applied. The $CoFe_2O_4$ nanoparticles (500 mg) were heated with oleic acid (168 µl) in octadecene (50 ml) at 95 °C for 4 h, and the resulting oleic acid-capped particles were dispersed in cyclohexane (50 ml). In a separate flask, glacial acetic acid (10 ml), barium acetate (544 mg), and titanium butoxide (729 µl) were mixed and heated to 95 °C. Then, the suspension of $CoFe_2O_4$ particles in cyclohexane was added dropwise, which was followed, after 15 min, by addition of butanol (20 ml) and heating for further 4 h. The suspension was transferred to an evaporating dish, carefully heated, and dried. The material was calcined at 400 °C, and thermal treatment in air at 700 °C for 2 h followed.

The raw $CoFe_2O_4$@$BaTiO_3$ nanomaterial was subjected to mechanical processing by rolling and mixer milling to break sintering bridges (see, e.g., [12]). The particles were then stabilized with ammonium citrate according to the procedure in [13] and were subsequently dispersed in ethylene glycol – water mixture with a volume ratio of 1 : 1. Mild mass fractionation was applied by means of centrifugation at 116 RCF for 10 min, and the supernatant containing a fine fraction of particles was isolated. The suspension was concentrated by exhaustive centrifugation, and the concentration of $CoFe_2O_4$@$BaTiO_3$ particles in the final ink was determined to 28.6 mg ml^{-1} by magnetometry of a dried aliquot.

2.2. Selected characterizations of the nanoparticles

The basic characterization of prepared nanomaterials included powder X-ray diffraction (XRD) with Cu Kα radiation, measured on a Bruker D8 Advance diffractometer, and SQUID magnetometry with a Quantum Design MPMS XL. The XRD measurement of the hydrothermal $CoFe_2O_4$ particles evidenced the single-phase character of the product, and the analysis of the diffraction line broadening by the Rietveld method provided the mean size of crystallites of 9 nm. The XRD analysis of the raw $CoFe_2O_4$@$BaTiO_3$ product confirmed the presence of both the spinel ferrite and $BaTiO_3$ perovskite phases (**Figure 1A**). Magnetization of the bare $CoFe_2O_4$ nanoparticles at 7 T and 5 K was 81.6 A m^2 kg^{-1} (see also hysteresis loops in **Figure 1B**), while the $CoFe_2O_4$@$BaTiO_3$ particles were characterized by magnetization of 36.7 A m^2 kg^{-1}, which indicated the ferrite content of 45 wt% in the product.

The hydrodynamic size of particles in the ink was probed by dynamic light scattering (DLS) at 25 °C by a Malvern Zetasizer Nano ZS. The ink was diluted by the water-ethylene glycol mixture (1:1) to two different concentrations (0.07 and 0.19 mg/mL), for which three measurements were performed. All measurements provided similar Z-average values of ≈ 129 nm and a polydispersity index of 0.19-0.23. Representative hydrodynamic size distribution, including different types of weighting, is shown in **Figure 1C**.

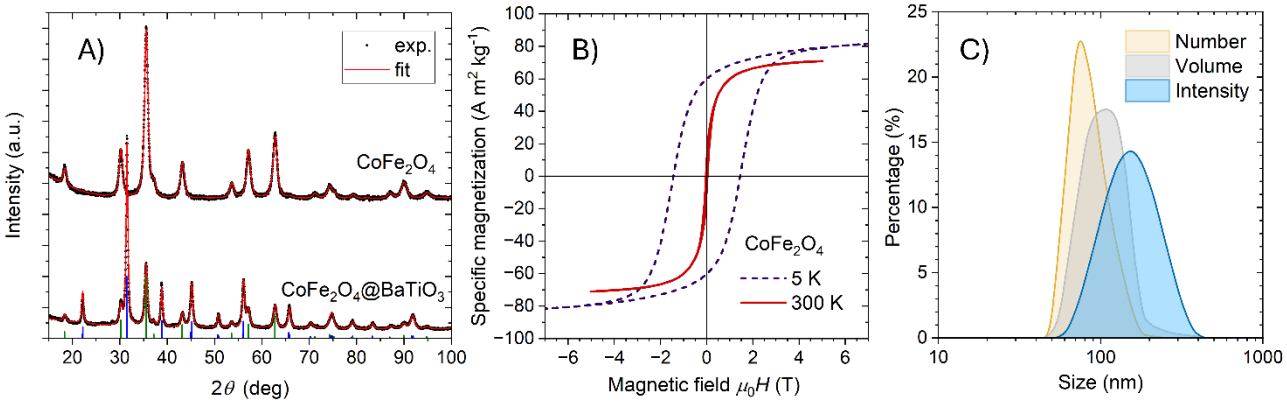

Figure 1 Basic characterization of the particles and the ink - A) Diffractograms (black) of the bare CoFe2O4 particles and raw CoFe2O4@BaTiO3 nanomaterial, complemented by patterns calculated by the Rietveld method (red). Diffraction lines of the CoFe2O4 ferrite with the spinel structure ($\boldsymbol{Fd\bar{3}m}$) and tetragonal BaTiO3 with the perovskite structure ($\boldsymbol{P4mm}$) are indicated by green and blue vertical bars. B) Magnetic hysteresis curves of the bare ferrite cores at 5 K and 300 K. C) Intensity, volume, and number-weighted hydrodynamic size distributions of particles in the CoFe2O4@BaTiO3 ink, as obtained from DLS.

2.3. Substrate

Two types of substrates were selected for overprinting: (i) a 1 mm thick glass slide from Ossila [14] with the dimensions of 20 mm x 15 mm, and (ii) a 140 µm thick polyethylene terephthalate (PET) mesoporous flexible foil from Mitsubishi NoveleTM IJ-220 by Novacentrix [15], stored in the roll.

2.4. Test structure fabrication

The test structures were fabricated using a piezoelectric inkjet printer (Fujifilm Dimatix DMP-2831, DMC-SAMBA cartridge) equipped with a single 17 µm nozzle. Printing was performed at resolutions of 1270 dpi, 1680 dpi, and 2540 dpi, corresponding to drop spacings of 20 µm, 15 µm, and 10 µm, respectively. Each test pattern consisted of a 1 mm × 1 mm square printed with 5, 10, and 20 overprinted layers on both glass slides and flexible PET substrates (**Figure 2**). The substrate temperature was maintained at 50 °C during printing to ensure stable droplet formation, controlled spreading, and uniform solvent evaporation. After deposition, the printed samples were dried in air at 80 °C for 30 min, followed by annealing at 150 °C for 1 h to enhance adhesion and remove residual solvents.

3. RESULTS AND DISCUSSION

The morphology and topography of the deposited MENP layers were characterized by optical microscopy, profilometry, and atomic force microscopy (AFM). **Figure 3** shows printed structures on PET, while **Figure 4** presents corresponding layers on glass substrates. The film thickness increased almost linearly with the number of printed layers, and higher printing resolutions led to smoother and denser morphologies due to improved droplet overlap. AFM analysis (performed on area of 50 µm x 50 µm) revealed root-mean-square roughness (R_{rms}) values ranging from 44 nm to 117 nm, depending on substrate and printing parameters. The lowest R_{rms} ≈ 44 nm was observed for 2540 dpi and 10 layers on glass, while the highest R_{rms} ≈ 117 nm corresponded to 1270 dpi and 5 layers on PET. Our results suggest that both increased printing resolution and multilayer overprinting substantially enhance nanoparticle packing and surface uniformity.

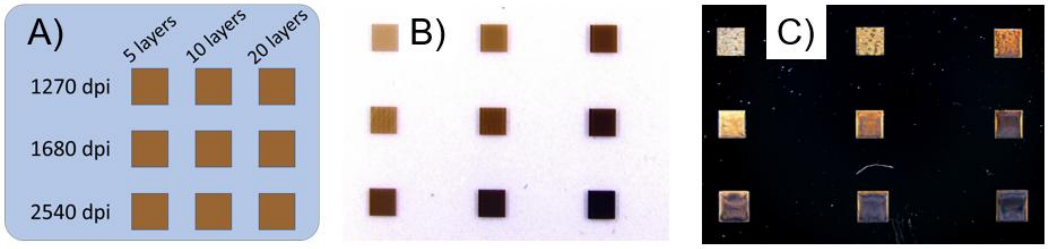

Figure 2 A) Printing parameters of printed test structures (1 mm × 1 mm) used for MENP deposition (resolution, layer count, substrate type), B) Printed structures on PET substrate, C) Printed structures on glass substrate.

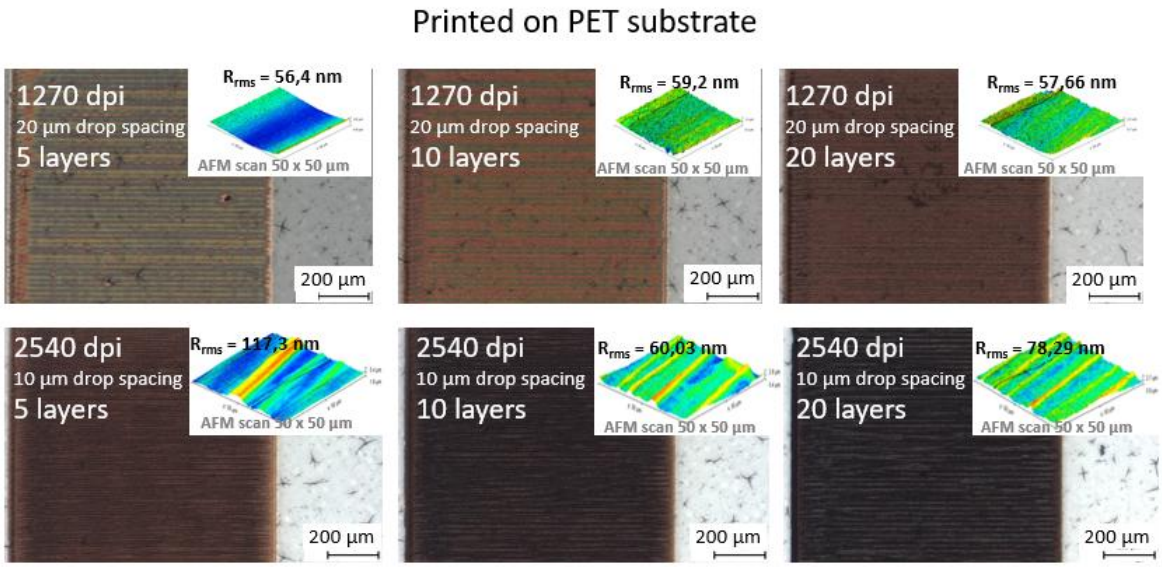

Figure 3. Optical micrographs and AFM topography of MENP layers on PET substrate. Structures (1 mm × 1 mm) were fabricated at 1270 dpi and 2540 dpi with 5, 10, and 20 printed layers. Scanned area in AFM: 50 µm x 50 µm.

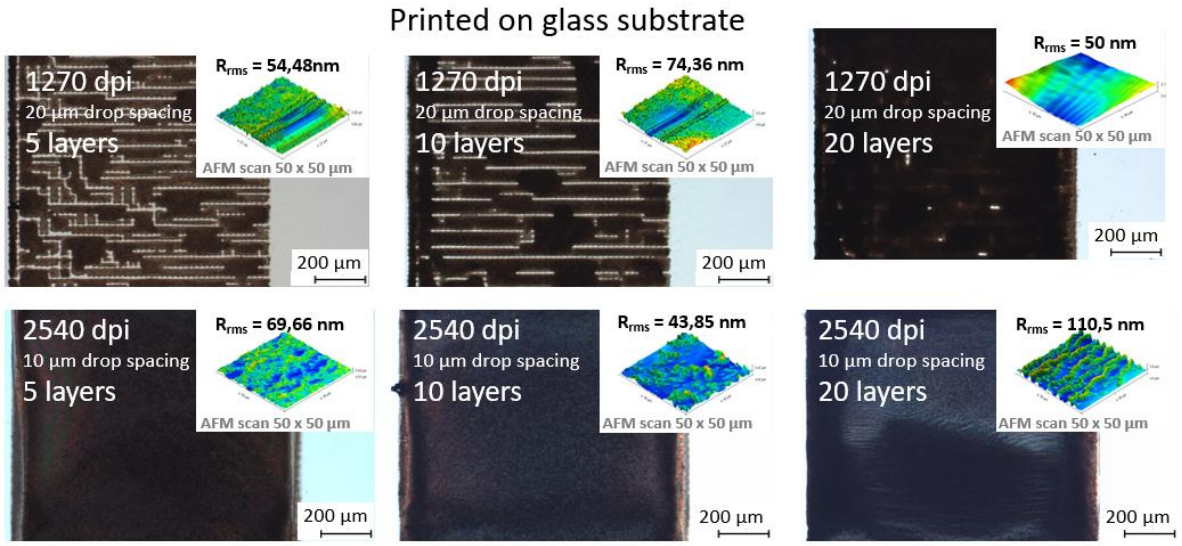

Figure 4 Optical micrographs and AFM topography of MENP layers (1 mm × 1 mm) printed on glass substrate at 1270 dpi and 2540 dpi with 5, 10, and 20 layers. Scanned area in AFM: 50 µm x 50 µm.

To further quantify the printed layer geometry, profilometric scans were performed for both PET and glass substrates (**Figure 5** and **Figure 6**). The measured thickness profiles follow the trend indicated in AFM data — the average film thickness increased almost linearly with the number of layers, from 0.9 µm (5 layers) to 1.7 µm (10 layers) and 4.0 µm (20 layers). The surface roughness remained below 2 µm across the printed area. The surface roughness remained below 2 µm across the printed area. However, on the PET substrate, a noticeable surface rippling was observed, with an amplitude of up to ±0.9 µm. This effect arises from the combination of inkjet printing parameters and the fast-drying nature of PET. When a droplet impacts the substrate, rapid solvent evaporation limits nanoparticle spreading, preventing the formation of a fully uniform surface. In contrast, films printed on glass substrates dried more slowly, allowing better leveling and smoother layer formation—particularly at higher resolutions (2540 dpi). Nevertheless, two additional phenomena were identified on glass. At lower resolution (1270 dpi), isolated uncovered dots appeared, likely due to the limited wettability of the surface and the faster movement of the printhead, which causes the droplets to coalesce unevenly. At higher resolution (2540 dpi), the amount of deposited ink was sufficient to create a continuous layer; however, slower solvent evaporation promoted particle migration, leading to subtle non-uniformities across the printed region. Quantitative values of thickness and surface rippling are summarized in **Table 1** and **Table 2**, confirming consistent results for both substrates and printing reproducibility.

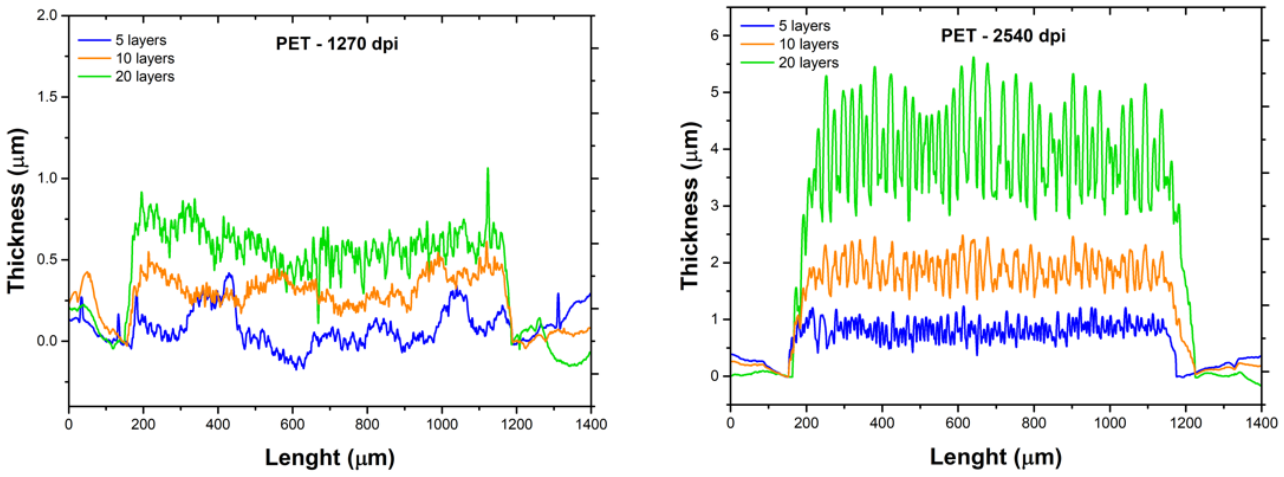

Figure 5 Measured thickness profiles of MENP layers at 1270 and 2540 dpi for 5, 10, and 20 printed layers on PET substrates. Data were obtained from profilometric scans (1.4 mm length).

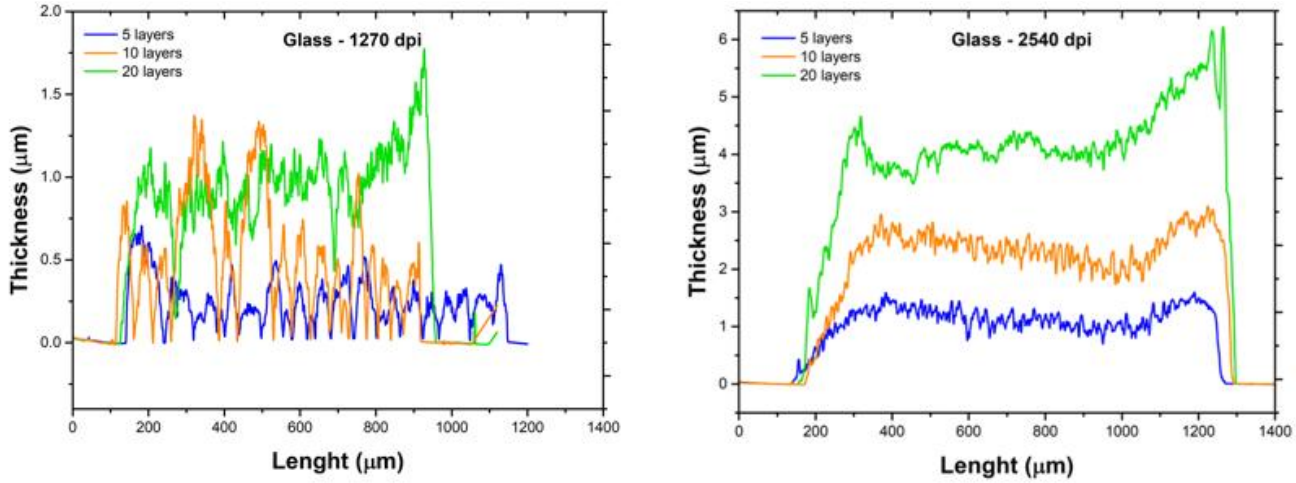

Figure 6 Measured thickness profiles of MENP layers at 1270 and 2540 dpi for 5, 10, and 20 printed layers on a glass substrate. Data were obtained from profilometric scans.

Table 1 Measured film thickness and surface rippling amplitude for printed MENP layers on PET substrate.

	Film thickness / rippling on PET		
# layer/ resolution	**1270 dpi**	**1680 dpi**	**2540 dpi**
5 layers	0.1 ± 0.1 µm	0.4 ± 0.1 µm	0.9 ± 0.15 µm
10 layers	0.2 ± 0.1 µm	0.8 ± 0.1 µm	1.7 ± 0.8 µm
20 layers	0.6 ± 0.25 µm	1.3 ± 0.25 µm	4.0 ± 0.9 µm

Table 2 Measured film thickness and surface rippling amplitude for printed MENP layers on glass substrate.

	Film thickness on glass		
# layer/ resolution	**1270 dpi**	**1680 dpi**	**2540 dpi**
5 layers	0.2 ± 0.08 µm	0.7 ± 0.1 µm	1.0 ± 0.2 µm
10 layers	0.5 ± 0.08 µm	1.1 ± 0.1 µm	2.2 ± 0.2 µm
20 layers	1.0 ± 0.1 µm	1.8 ± 0.1 µm	4.0 ± 0.05 µm

4. CONCLUSION

This study presented the fabrication and detailed morphological characterization of inkjet-printed MENP films on rigid (glass) and flexible (PET) substrates. By varying the printing resolution (1270–2540 dpi) and number of printed layers (5–20), correlations were established between deposition parameters, film thickness, and surface roughness. For the PET substrate, at low resolution (1270 dpi) the effective layer thickness could be reliably measured only for samples with 10 or more printed layers, as the porosity of the substrate strongly influenced the data for thinner films. At higher resolutions (2540 dpi), an almost linear relationship between thickness and layer count was observed, accompanied by a uniform average film thickness for each configuration. However, a noticeable surface rippling with an amplitude of up to ±0.9 µm appeared, particularly for thicker films. This effect could potentially be mitigated by alternating the printing direction during deposition. In contrast, films printed on glass substrates exhibited significantly lower rippling (up to ±0.2 µm) but showed stronger effects related to surface wettability and slower solvent evaporation. These factors resulted in uncovered areas at low resolution (1270 dpi) and non-uniform coverage at high resolution (2540 dpi).

The film thickness across all samples ranged from 0.1 µm to 4.0 µm, while the measured root-mean-square roughness (R_{rms}) varied between 43 nm and 117 nm, depending on resolution, substrate, and number of layers. Printing time also represents an important process factor: one layer required approximately 15 minutes at 1270 dpi and 30 minutes at 2540 dpi. Therefore, the optimal thickness for a given application must represent a balance between film quality and production time. Based on the obtained results, a practically usable film thickness of around 1 µm was identified, achievable with 10 layers at 1270 dpi on PET.

The choice of a specific substrate will depend on the final application, of course. Both selected materials can be printed on without prior surface treatment of the substrate. However, glass exhibits greater potential for use in further MENP measurements of materials in high/low temperature environments to determine the magnetoelectric effect. With high-resolution printing, a higher density of the applied layer can be achieved while maintaining reasonable waviness (up to 4.0 ± 0.05 µm).

ACKNOWLEDGEMENTS

This work was supported by the Czech Science Foundation project no. 25-16615S, by the Czech Technical University Student Grant No. SGS23/182/OHK3/3T/13 and by the MEYS grant LM2023051. We would like to thank our colleague Jarmila Kuličková for her help during the preparation of MENPs employed in this study.

REFERENCES

[1] N. A. SPALDIN and M. FIEBIG. “The Renaissance of Magnetoelectric Multiferroics.” *Science (80-.).* Jul. 2005, vol. 309, no. 5733, pp. 391–392, doi: 10.1126/science.1113357.

[2] C.-W. NAN, M. I. BICHURIN, S. DONG, D. VIEHLAND and G. SRINIVASAN. “Multiferroic magnetoelectric composites: Historical perspective, status, and future directions.” *J. Appl. Phys.* Feb. 2008, vol. 103, no. 3, doi: 10.1063/1.2836410.

[3] J. MA, J. HU, Z. LI, and C. NAN. “Recent Progress in Multiferroic Magnetoelectric Composites: from Bulk to Thin Films.” *Adv. Mater.* Mar. 2011, vol. 23, no. 9, pp. 1062–1087, doi: 10.1002/adma.201003636.

[4] V. ANNAPUREDDY *et al.* “Magnetic energy harvesting with magnetoelectrics: an emerging technology for self-powered autonomous systems.” *Sustain. Energy Fuels*. 2017, vol. 1, no. 10, pp. 2039–2052, doi: 10.1039/C7SE00403F.

[5] C. SONG, B. CUI, F. LI, X. ZHOU, and F. PAN. “Recent progress in voltage control of magnetism: Materials, mechanisms, and performance.” *Prog. Mater. Sci.* Jun. 2017, vol. 87, pp. 33–82, doi: 10.1016/j.pmatsci.2017.02.002.

[6] B. LUO *et al.* “Magnetoelectric microelectromechanical and nanoelectromechanical systems for the IoT.” *Nat. Rev. Electr. Eng.* May 2024, vol. 1, no. 5, pp. 317–334, doi: 10.1038/s44287-024-00044-7.

[7] Y.-W. FANG *et al.* “First-principles studies of multiferroic and magnetoelectric materials.” *Sci. Bull.* Jan. 2015, vol. 60, no. 2, pp. 156–181, doi: 10.1007/s11434-014-0628-4.

[8] M. KUJAWSKA and A. KAUSHIK. “Exploring magneto-electric nanoparticles (MENPs): a platform for implanted deep brain stimulation.” *Neural Regen. Res.* 2023, vol. 18, no. 1, p. 129, doi: 10.4103/1673-5374.340411.

[9] N. ORTEGA, A. KUMAR, J. F. SCOTT, and R. S. KATIYAR. “Multifunctional magnetoelectric materials for device applications.” *J. Phys. Condens. Matter*. Dec. 2015, vol. 27, no. 50, p. 504002, doi: 10.1088/0953-8984/27/50/504002.

[10] Y.-J. WANG *et al.* “Flexible magnetoelectric complex oxide heterostructures on muscovite for proximity sensor.” *npj Flex. Electron.* 2023, vol. 7, no. 1, p. 10, Feb. doi: 10.1038/s41528-023-00241-8.

[11] K. L. KOZIELSKI *et al.* “Nonresonant powering of injectable nanoelectrodes enables wireless deep brain stimulation in freely moving mice.” *Sci. Adv.* Jan. 2021, vol. 7, no. 3, doi: 10.1126/sciadv.abc4189.

[12] O. KAMAN *et al.* “The magnetic and hyperthermia studies of bare and silica-coated La0.75Sr0.25MnO3 nanoparticles.” *J. Nanoparticle Res.* Mar. 2011, vol. 13, no. 3, pp. 1237–1252, doi: 10.1007/s11051-010-0117-x.

[13] O. KAMAN *et al.* “Silica encapsulated manganese perovskite nanoparticles for magnetically induced hyperthermia without the risk of overheating.” *Nanotechnology*. Jul. 2009, vol. 20, no. 27, p. 275610, doi: 10.1088/0957-4484/20/27/275610.

[14] Ossila unpaterned ultrafalt glass slide, online. 2025 [viewed: 2025-10-15]. Available from: https://www.ossila.com/products/ito-glass-substrates-unpatterned

[15] Novacentrix PET-based substrate, online. 2015. [viewed: 2025-10-15]. Available from: https://novacentrix.com/datasheet/Novele IJ-220.pdf